PROCEEDINGS A

rspa.royalsocietypublishing.org

Research

Cite this article: Zeng F, Jiang MQ, Dai LH. 2018 Dilatancy induced ductile–brittle transition of shear band in metallic glasses. *Proc. R. Soc. A* **474**: 20170836. http://dx.doi.org/10.1098/rspa.2017.0836

Received: 29 November 2017
Accepted: 12 March 2018

Subject Areas:
materials science, mechanical engineering, mechanics

Keywords:
shear bands, dilatancy, cutting, ductile–brittle transition, metallic glass

Author for correspondence:
L. H. Dai
e-mail: lhdai@lnm.imech.ac.cn

Dilatancy induced ductile–brittle transition of shear band in metallic glasses

F. Zeng[1,2], M. Q. Jiang[1,3] and L. H. Dai[1,3]

[1]State Key Laboratory of Nonlinear Mechanics, Institute of Mechanics, Chinese Academy of Sciences, Beijing 100190, People's Republic of China
[2]Software Center for High Performance Numerical Simulation, Chinese Academy of Engineering Physics, Beijing 100088, People's Republic of China
[3]School of Engineering Science, University of Chinese Academy of Sciences, Beijing 101408, People's Republic of China

LHD, 0000-0001-7772-3504

Dilatancy-generated structural disordering, an inherent feature of metallic glasses (MGs), has been widely accepted as the physical mechanism for the primary origin and structural evolution of shear banding, as well as the resultant shear failure. However, it remains a great challenge to determine, to what degree of dilatation, a shear banding will evolve into a runaway shear failure. In this work, using *in situ* acoustic emission monitoring, we probe the dilatancy evolution at the different stages of individual shear band in MGs that underwent severely plastic deformation by the controlled cutting technology. A scaling law is revealed that the dilatancy in a shear band is linearly related to its evolution degree. A transition from ductile-to-brittle shear bands is observed, where the formers dominate stable serrated flow, and the latter lead to a runaway instability (catastrophe failure) of serrated flow. To uncover the underlying mechanics, we develop a theoretical model of shear-band evolution dynamics taking into account an atomic-scale deformation process. Our theoretical results agree with the experimental observations, and demonstrate that the atomic-scale volume expansion arises from an intrinsic shear-band evolution dynamics. Importantly, the onset of the ductile–brittle transition of shear banding is controlled by a critical dilatation.

THE ROYAL SOCIETY PUBLISHING

1. Introduction

Amorphous materials include a wide range of systems, including granular materials, glasses and colloids. These materials often undergo a localized deformation in narrow shear zones, ranging in scale from atomically thin bands to the natural faults of the Earth's crust [1–7]. In the structural geology, shear bands show apparent evidence of the both ductile and brittle deformation process, and are generally classified into three types via the distance to earth surface, such as upper brittle shear bands (less than 8–10 km) generating a clear discontinuity, lower ductile shear bands bearing ductile flow (greater than 15 km) and the brittle–ductile shear bands inheriting both deformation features in the middle zone [8,9]. While shear bands developed in glassy materials and the Earth's crust differ vastly in scale, each is made up of a collection of smaller particles, where the glassy band structure contains a few layers of molecules, while the earthquake fault is filled with crushed grains of rock. Shear bands in these systems exhibit similar and complex dynamics, including the brittle and ductile deformation features, strongly dependent on the microstructure within bands and the constraint applied on the bands. However, it is difficult to experimentally track any underlying microscopic mechanisms during the evolution of shear bands due to strong localization in both space and time. This dilemma particularly stands out in metallic glasses (MGs), a new class of atomic-disordered materials that have gained much attention due to their attractive and unique properties. In MGs, shear bands are only a few hundreds of atoms thin and believed to operate fast in less than a few milliseconds [10–12]. In this paper, we develop an ingenious experiment coupling the severe plastic deformation (SPD) process for MGs with the *in situ* acoustic emission (AE) monitoring. Based on this, we reveal a scaling law of atomically structural change proportional to the evolution degree of shear bands, and further attempt to theoretically bridge the microstructure and the ductile or brittle behaviours of shear bands.

Dilatancy as a representative structural change is a universal feature of deformation of dense amorphous materials in response to shear. Earlier, the dilatancy of granular material was studied by Osborne Reynolds who noted the disappearance of water under footsteps while walking along a wet beach [13]. Now, this property is of particular importance in MGs. In crystalline metals, deformation at constant volume owing to the periodicity along the slip plane provides identical atomic positions for the sheared material. This situation, however, is not available in MGs. A sheared portion of MGs does not find such a perfect fit and must leave some holes [14,15]. It is generally recognized that the fundamental unit process underlying deformation of MGs must be a local rearrangement of atoms that can involve dilatancy and accommodate shear strain. Several theoretical models were proposed over the past decades, providing a comprehensive interpretation of the shear-induced dilatancy feature in the plastic deformation of MGs. For example, the free volume model proposed by Spaepen [14] ascribes the shear flow to the creation of free volume via the atomic-scale dilatation effect. Argon [16] suggested that amorphous plasticity results from the accumulation of shear transformations zones (STZs) occurring within defective regions few to hundreds of atoms wide; the net effect of STZs is an excess dilatation that must create at least temporarily additional excess free volume [3,17]. Considerable works have demonstrated the inherent shear-dilatation coexistence during deformation of MGs by experiments [18] and simulations [19].

At temperatures well below the glass transition temperature, the plastic deformation of MGs is prone to be highly localized into shear bands [20–24]. Many works focus on the nucleation and evolution of shear bands. Gao developed a finite-element scheme to model the individual processes of shear bands based on the free-volume model [25]. Subhash and co-workers investigated the evolution of a shear band via the thermomechanical model that took into account the free volume theory [20,26]. It has been generally accepted that atomic-level volume dilatation, which generates structural softening and leads to a precipitous drop in viscosity, is the origin of shear bands and also dominates their evolution process, where the temperature rise just plays a secondary role [11,20,27–29]. Therefore, understanding structural changes within shear bands holds the key to unveil the shear-banding dynamics. In this aspect, early attempts

were done by direct structural imaging of shear bands using transmission electron microscopy (TEM), or by detecting changes in density in severely deformed specimens. These studies usually suggest the dilatancy in the form of free volume or density as the primary structural change within shear bands [23,30–35]. The detailed study of the internal structure of individual shear bands was performed by Donovan & Stobbs [30] via TEM. They found that there is a change in the average inter-atomic spacing in the shear band, corresponding to the free volume coalescence or the density decrease. Wilde *et al*. revealed that the shear band shows a spectrum of densities with an average decrease compared to the matrix of about 2.9% [31,32], and Liu *et al*. found that the density change between the matrix and shear band ranges from −1 to −12% [35], by using the high-angle annular dark-field scanning TEM signal. Pan *et al.* reported that a dilatation of approximately 1.14% was obtained in a ZrCuNiAl MG by detecting changes in density in severely deformed specimens [23]. Moreover, higher dilatation of 15% [33] and 20% [34] were measured, respectively. These measured results of the dilatation values show a significant scatter ranging from 1% up to 20%. This implies that the shear-band dilatancy strongly depends on the developed stages of shear banding and is also highly material-specific, as demonstrated theoretically by Jiang *et al.* [36]. The volume change in shear bands is of character accumulated as a function of shear displacement of shear bands, which is reflected as atomic-scale free-volume increase in embryonic shear bands, and coalesces into non-voids in mature shear bands, as experimentally shown by Yao and co-workers [37], and as simulated by Zhang and co-workers [38]. Recently, the underlying mechanism of how nano-voids nucleate and grow, i.e. cavitation, in MGs has been extensively investigated by Li and co-workers [39]. It is suggested that, depending on the dilatancy degree within bands, shear bands can display a local ductile flow behaviour, alternatively can lead to the catastrophic failure with a brittle feature, showing a dilatancy-induced ductile-to-brittle transition of shear banding. Nevertheless, the above studies could not address the key questions of primary scientific interest as to the dilatancy evolution at the different stages of individual shear band and the critical degree of dilatancy that is required to induce the transition of shear banding.

It is clear that resolving the correlation between the dilatancy level and the evolution degree of shear banding requires an experimental technique to accurately control the developed stages of shear bands, and meanwhile to directly probe the fast and collective volume change within the bands. Many researchers have tried to investigate shear bands through bending, indentation, uniaxial compression, high-pressure torsion and cold-rolling. These methods, however, are very difficult to control the degree of deformation within shear bands. Alternatively, the SPD techniques such as cutting effectively control the shear-band deformation [40–43]. Guo *et al*. investigated the flow dynamics of shear bands in cutting and sliding of metals via varying the indenter rake angle from large negative to positive values [40,41]. Mahato and co-workers revealed that the shear-band flow can unfold in two phases: an initiation phase which creates a localized weak zone, followed by a viscous sliding phase across this zone that results in large localized strains [42]. Most importantly, the evolution degree of shear bands can be well controlled by tuning individually several control parameters including cutting depth, cutting speed and tool geometry. Cutting as a successful technology is widely applied to study adiabatic shear bands in crystalline alloys [41,44–47]. The onset criterion of adiabatic shear bands in crystalline alloys was firstly obtained by Recht from cutting experiments of titanium [44]. In particular, the evolution degree of adiabatic shear bands can be controlled via varying the cutting speed or depth [45,46]. In this work, we will show that the cutting method developed previously is still valid to control the evolution process of nano-scale thick shear bands in MGs. As for how to capture the structural change in shear bands, an *in situ* AE can achieve this, which has been widely used in detection of material defects [48,49].

In this work, an ingenious method consisting of cutting-SPD and *in situ* AE, which can monitor the evolution of structural dilatation during shear banding, is applied to investigate the characterization of dilatancy as well as its correlation to the evolution degree and ductile-to-brittle transition of shear bands. A scaling law is observed that the dilatancy is linearly related to the evolution degree of a shear band. We develop a theoretical model of shear-band

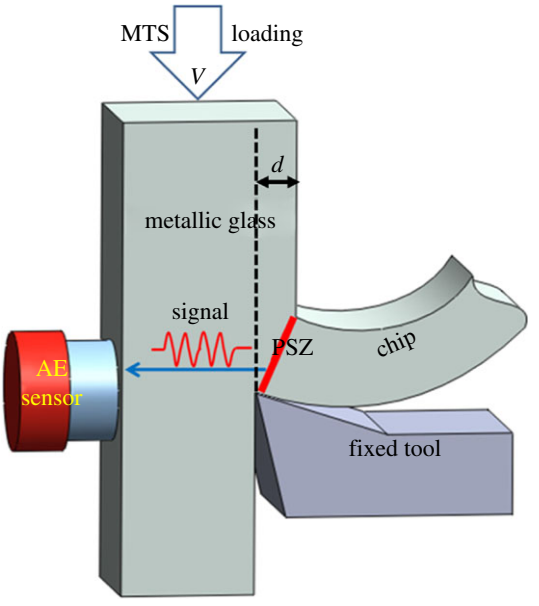

Figure 1. Schematic for the severe plastic deformation of MGs under the controlled machining technology with an AE sensor.

evolution, which bridges the atomic-scale deformation process and the macroscopic shear-band behaviour. It is further demonstrated that the ductile-to-brittle transition of shear bands is due to the structural dilatancy. These findings have potential benefits for a deep understanding of shear-band dynamics of atomic-disordered materials.

2. Experimental procedure

Master alloy ingots with the nominal composition $Zr_{41.2}Ti_{13.8}Cu_{12.5}Ni_{10}Be_{22.5}$ (Vitreloy 1) were prepared by arc-melting the elements Zr, Ti, Cu, Ni and Be (with a purity of 99.9% or better) together in a Ti-gettered high-purity argon atmosphere. Glassy rods ($\Phi 10 \times 60$ mm) were prepared by suction casting in water-cool Cu moulds and subsequently cut into samples ($5 \times 5 \times 30$ mm). Figure 1 shows the device machining of MGs which is conducted on material test machine 810 [50]. Here, an orthogonal machining process is taken into consideration, where a wedge-shaped tool is fixed, and the workpiece with a cutting depth d is moving towards the tool at the cutting speed V. During machining, the cutting speed V of 10 µm s^{-1} is fixed and controlled by the MTS-810, and the alterable cutting depth controlled by the locating device is 50, 65, 75, 90, 150 and 220 µm, respectively. A broadband (100–1000 kHz) piezo-electric AE-sensor WD (Physical Acoustic Corporation, USA) was used to capture the shear-band signals. Since the AE sensor cannot be directly mounted on the MG workpiece, a waveguide was used to connect the AE sensor with the workpiece. The load signal was recorded by MTS-810, while a continuous AE-stream was sampled at 2 MHz by using a high-resolution 18-bit PCI-2 AE board (Physical Acoustic Corporation, USA).

3. Experimental results

(a) Shear-band evolution dependence of serrated flow

Figure 2 presents cutting force–displacement curves and the corresponding chip morphologies at different cutting depths from 50 to 150 µm. The Vitreloy 1 MGs approximately exhibit an ideal elasto-plastic behaviour, where a serrated flow occurs and its serration amplitude of the cutting force increases with increasing cutting depth (figure 2*a*). The serrated flow is widely observed in

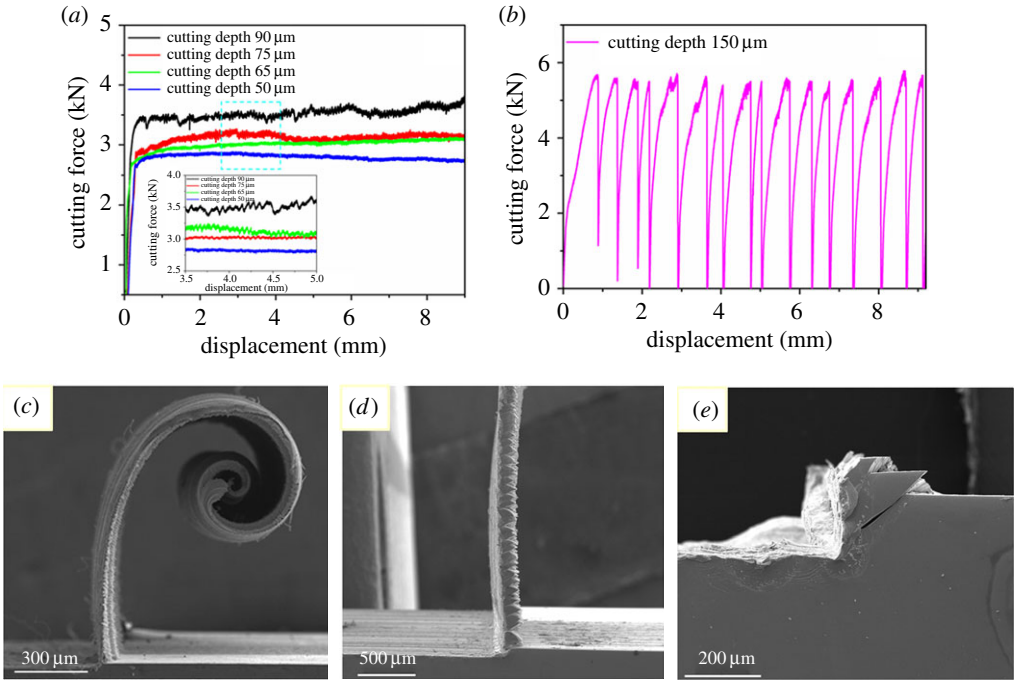

Figure 2. Cutting force–displacement curves (*a*,*b*) and the chip morphologies (*c*–*e*) corresponding to the depth of 50, 90 and 150 µm, respectively.

the load-constraint deformation such as compressions and indentations. However, the serrated flow is greatly different between machining and compressions/indentations. As indicated in figure 1, the MG cutting occurs by a concentrated shear along a distinct narrow region which is approximately planar, called the primary shear zone (PSZ); this extends from the cutting edge to the work surface ahead of the tool and is inclined at an angle. The material is unstressed and does not deform until it enters the PSZ. As it approaches this thin layer, the stress in the material builds up rapidly. The shear strain is initially elastic, but the yield stress is exceeded quickly and the plastic flow sets in. The shearing within the PSZ, leads to a decrease of cutting force due to kinetic softening of the shear band, and a chip separates from the workpiece and moves up along the face of the tool. The shear banding would arrest as it is taken away from the PSZ by the chip flow. When the new material enters into the PSZ again, the cutting force increases and the new shear-band operation with initiation, propagation and arrest will reoccur. Therefore, it is believed that serrated flow behaviour of MGs is attributed to the repeated shear-band processes and the degree of serrated flow is dependent on shear-band evolution [45]. As the cutting depth increases, a transition from the stable to unstable serrated flow is observed, as well as a transition of chip morphologies from continuous to discontinuous chips as shown in figure 2*b*,*e* at 150 µm depth of cut. Similar result is also found in the case of 220 µm. As the chip morphologies containing the serrations and its characteristic sizes is largely related to the shear-band evolution dynamics in PSZ [46], a scanning electron microscope was used to characterize the chip morphologies to uncover the correlation between shear banding and serrated flow.

Figure 3*a* displays typical serrated chips morphology during machining of Vitreloy 1 MGs at 90 µm depth of cut. It can be clearly seen that serrations are nearly periodic with constant spacing on the micrometre scale in figure 3*b*. Figure 3*c* presents a high-magnification micrograph of an area marked 'I' in figure 3*b*, showing that primary shear bands characterize serrated chips and secondary shear bands lay between serrations. Figure 3*d* is the free surface of chips, as right-side view of chips in figure 3*a*. Interestingly, a regular lamellar structure with a constant spacing of several micrometres (figure 3*e*,*f*) clearly emerges. Furthermore, no characteristic

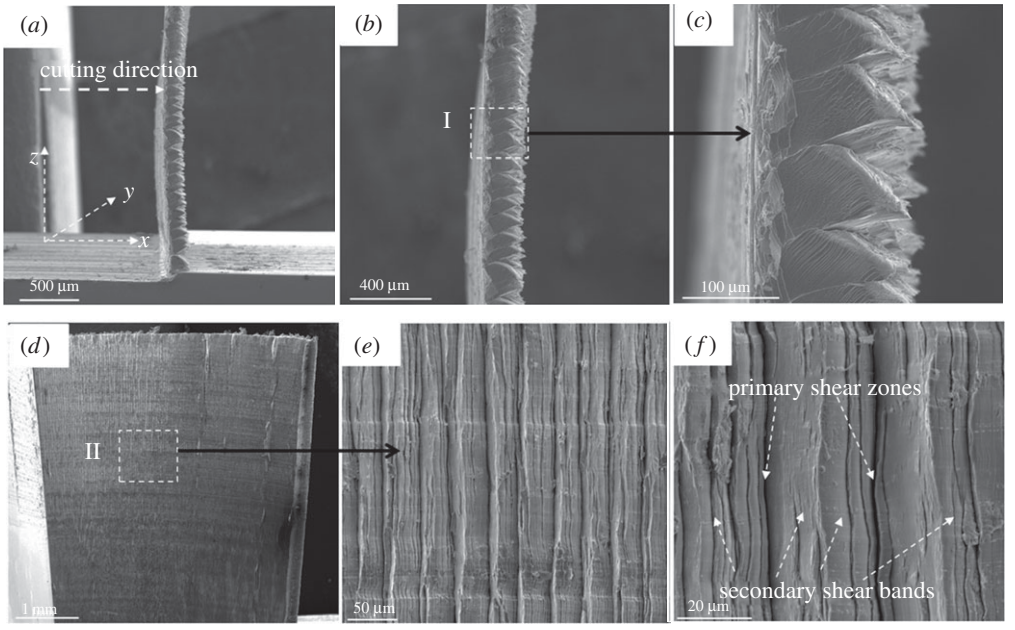

Figure 3. (*a*) The typical serrated chip morphology of Vitreloy 1 MG at a 90 µm depth of cut; (*b*) enlarged view of the chip; (*c*) details corresponding to square 'I' in (*b*); (*d*) the right-side view of the chip; (*e*,*f*) details corresponding to square 'II' in (*d*) at different magnification.

fracture patterns, such as vein-pattern and dimple, are observed on both surfaces of this lamellar chip. It is reasonable to conclude that the serrated chips result from periodic primary shear-banding processes, originating at the tool-contact surface, quickly propagating towards the free surface (figure 3*d*) and subsequently shearing in a simultaneous fashion in the PSZ (as marked in figure 3*f*). From the viewpoint of phenomenology, the serrated chips during MG machining are very similar to the formation of serrated chips in crystalline alloys. Both of types of chip form via repeated shear banding in the PSZ due to the interplay of tool and workpiece. As for the crystalline alloys, the serrated degree of chips is dependent on the cutting depth. Here a similar result is obtained for MGs. Figure 4 shows a clear increase in the degree of serrations with increasing cutting depth at a fixed cutting speed. A recognizable serration usually corresponds to a shear-banding event, which is confirmed in compression [23] and bending [21]. During the serrated chip formation, a serration is distinctly distinguished by an obvious shear step. Therefore, it is reasonable to believe that one primary shear-band forms inside the PSZ and leads to an associated serration. The shear band could evolve to a certain degree before it is taken away from the PSZ due to the chip flow. Just because of the shear-band evolution, the shear front surface becomes visible, which makes the chip formation appearing to be serrated. The degree of serrations hence reflects the evolution degree of shear bands. Meanwhile, the evolution degree of shear bands can also be represented by the spacing of serrations. Figure 5 shows the spacing of serrations increases with cutting depth, meaning the more developed shear bands. With the observation of the degree and spacing of serrations, tracking shear-band evolution in MGs is achieved via the controlled machining.

At the cutting depths from 50 to 90 µm, a stable serrated flow corresponding to the continuous chips is observed. However, as the depth reaches a certain value such as 150 or 220 µm, the chips become discontinuous, indicating instability of serrated flow as shown in figure 6. A potential underlying microscopic picture can be postulated by drawing an analogy to the deformation behaviour of shear bands in the structural geology. According to the deformation feature, a discontinuity exists in brittle shear bands, while the deformation is accomplished entirely by ductile flow in ductile shear bands [1,8,9]. In analogy to the transition from the continuous to

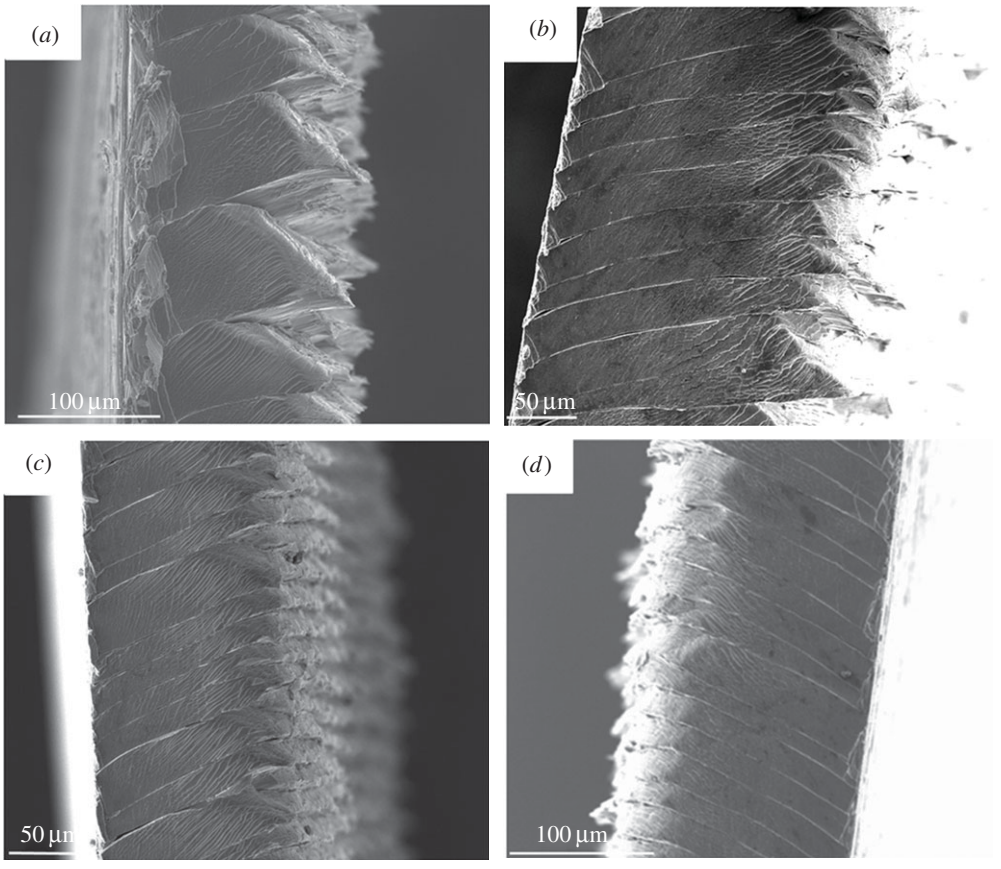

Figure 4. The typical serrated chips morphologies at the different cutting depths. (*a–d*) The depth of 90, 75, 65 and 50 µm, respectively.

discontinuous chips as MGs under machining, ductile shear bands induce stable serrated flow, while brittle shear bands as runaway shear failure give rise to the instability of serrated flow.

(b) Acoustic emission measurements

In situ AE testing provides a powerful method to gain further insight into the characterization of the shear-banding process in MGs [48,49]. A definitive method for evaluating the characteristic parameters of shear-band nucleation and propagation is still missing. In this regard, AE measurements may represent a potent alternative method because of their extremely high sensitivity with regards to the detection of elastic wave propagation by small-scale structural rearrangements and the high acquisition rates possible. Inspired by the previous work [49], an AE was used to capture the structural dilatancy associated with the shear-band evolution. During the machining of MGs, a primary shear band in the PSZ can be viewed as cooperative shearing process of a collection of STZs, where STZs change into a loose configuration with a larger volume, resulting in dilatancy [28]. Such rapid and local structural changes generate transient elastic waves that can be captured by the AE sensor, as shown in figure 7. An overview of AE signals and the corresponding cutting force curve at the cutting depth 75 µm are shown in figure 8*a*. Typical serrations are observed in the force signal, indicative of an intermittent, stick-slip like primary shear-band operation. Comparing the high AE signals to features in the force–time curves reveals a clear correlation between the occurrence of serrations and enhanced AE activities (figure 8*b*). Figure 8*c* is a close-up view of a single high signal shown in figure 8*a*. The main AE

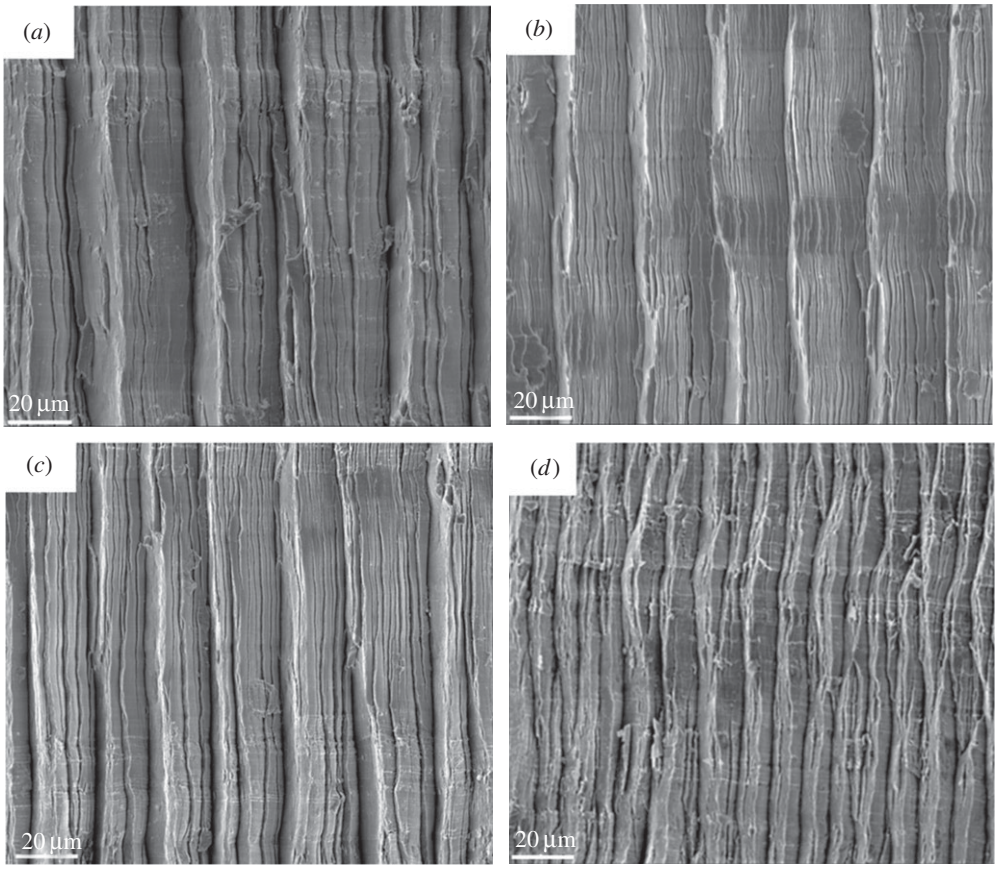

Figure 5. Free surface morphologies of chips at the different depths of cut. (*a–d*) The depth of 90, 75, 65 and 50 µm, respectively.

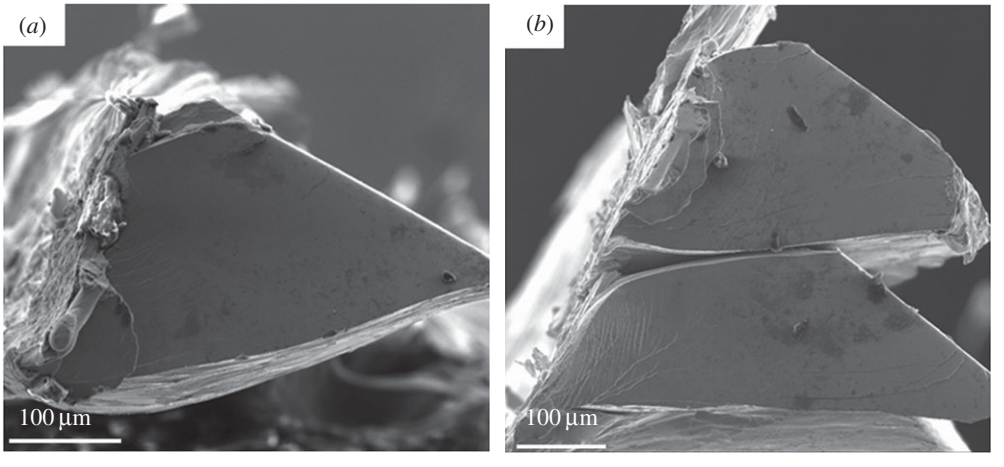

Figure 6. Morphologies of discontinuous chips at the depth of (*a*) 150 µm and (*b*) 220 µm.

signal shows a rise region with approximate time 100 µs. Continuous attenuation of the signal then follows, leading to a typical tail which is generally attributed to resonances within the sensor. Additionally, there are some low AE signals between the high signals, which correspond to the secondary shear bands. As for the other cases (50, 65 and 90 µm), the similar results are obtained

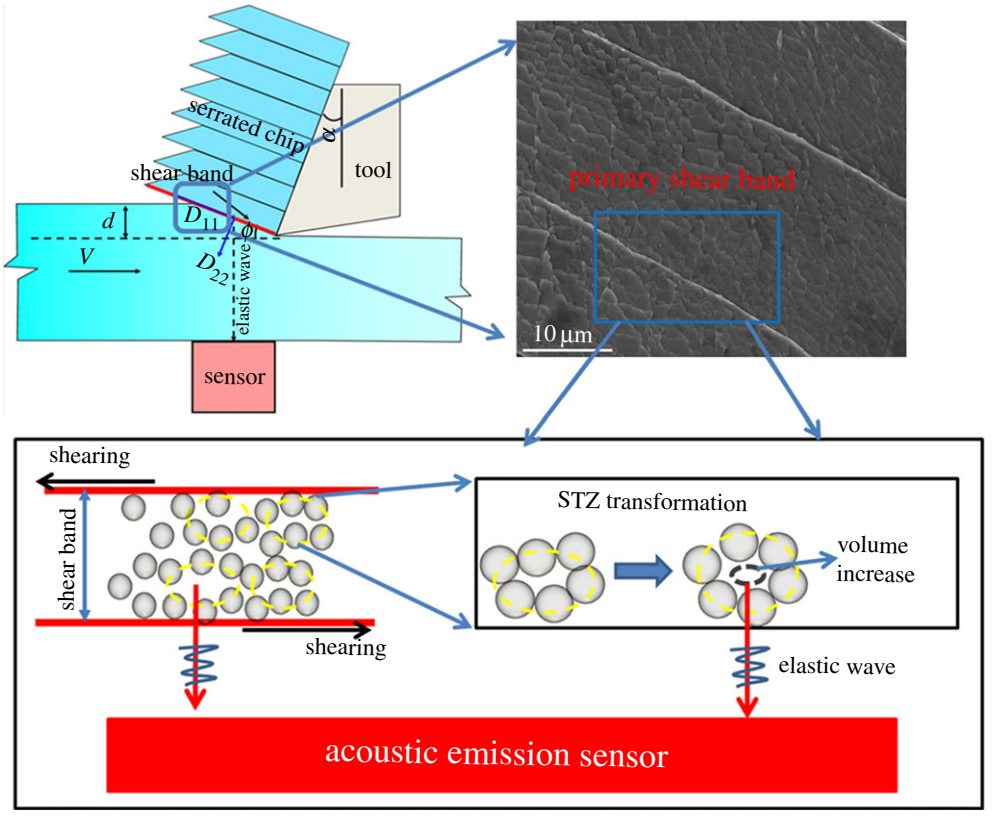

Figure 7. Schematic of the AE sensor capturing structural dilatancy during shear banding.

and not shown here. Abundant experiments and MD simulations capture free-volume evolution as the main picture of structural evolution in the shear-band process [18,19,25]. Therefore, it is reasonable to believe that structural evolution in both initiation and evolution of shear bands can be captured by AE monitoring.

The AE signal is attributed to a collective atomic-scale mechanism that induces a local volume expansion during shear banding. The analytical solution of shear-band dilatancy $\delta V/V$ with the associated AE signals is obtained

$$\frac{\delta V}{V} = \frac{(\pi c_1 r)(\lambda + 2G)}{\lambda + 2G/3} \frac{kU_p t_r}{2V}, \tag{3.1}$$

where the total volume change is δV normalized with respect to the volume V of primary shear band to determine the degree of shear-band dilatancy $\delta V/V$, c_1 is the compression wave speed, λ is Lamé's constant, G is the shear modulus, r is the distance from the dilatancy source to the AE monitoring, k is the sensor calibration factor used to convert the measured amplitude (in volts) into units of surface displacement (metres), U_p and t_r are the voltage and the rise time from the first threshold crossing to the peak amplitude as shown in figure 8*c*. The details of the solution are presented in appendix A.

Figure 9 shows histograms of values of shear-band dilatancy determined from hundreds of AE transients at the different cutting depths. Three-dimensional sizes of shear band are an assumed thickness of 15 nm [49], a width of 5 mm equivalent to the width of the MG workpiece and a length of $d/\sin\phi$, where d is the cutting depth and the rank angle is taken to be $\phi = 15°$ [45]. The rest of the calculated parameters are as follows: $\lambda = 90$ GPa, $\mu = 35$ GPa, $c_1 = 3950\ \mathrm{ms}^{-1}$, $r = 5$ mm and $k \sim 0.5 \times 10^{-12}\ \mathrm{m\,mv}^{-1}$. Using Gauss fit for histograms, the mean values of shear-band dilatancy are $14.6 \pm 0.4\%$, $11.9 \pm 0.2\%$, , $9.9 \pm 0.4\%$, and $8.2 \pm 0.3\%$, at corresponding depths of 90, 75, 65 and

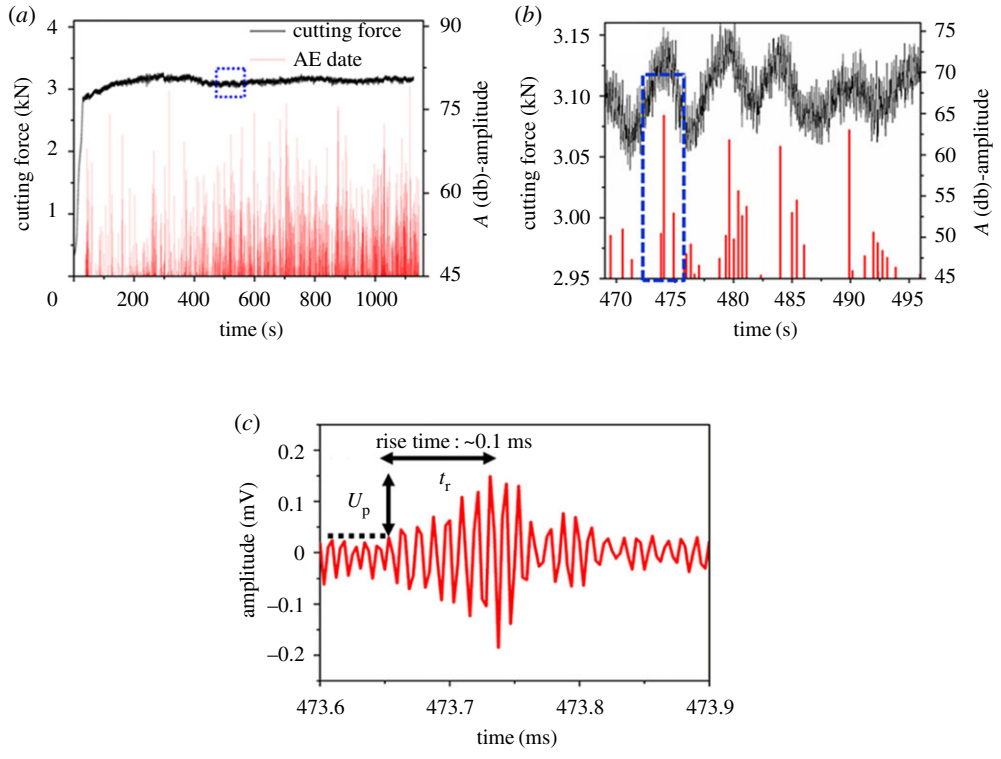

Figure 8. (*a*) Acoustic emission amplitude measured *in situ* during a machining test performed at 75 µm depth of cut. (*b*) Details corresponding to square in *a* on the variation of large acoustic emission amplitude in relation to the magnitude and presence of serrations. (*c*) An enlarged high signal in the squared area of *b*.

50 µm, respectively. As for the cases of depths of 150 and 220 µm, the continuous chips change into discontinuous chips and fracture generate giant overshooting signals, which seriously interferes with the signals of shear bands. A similar phenomenon can be also observed in MGs tested in tension [51]. Hence, the critical shear-band dilatancy close to fracture is obtained via a shear-band evolution model not AE signals, which will be discussed further below in detail. It is remarked that these values of dilatancy increase with the increase in cutting depth. Since the similar correlation between the evolution degree of shear bands and the cutting depth based on our experimental results, we can conclude that dilatancy increases with increasing the evolution degree of shear bands.

The rationality of shear-band dilatancy can be further supported by comparison with related work. A series of attempts were made to measure the shear-band dilatancy by detecting changes in density or structural imaging of shear bands using TEM were done. A dilatancy of approximately 15% has been obtained subjected to extensive inhomogeneous deformation due to rolling [33]. Moreover, a higher dilatancy of approximately 20% has been measured [34]. Meanwhile, Shao *et al*. [37] have observed a high-resolution TEM image of an amorphous shear band with two distinct grey and white zones, corresponding to 4.5 and 11.8% volume dilatation, respectively. Jiang *et al*. [36] have developed a model for predicting the shear-band dilatation and concluded that mature shear bands possess higher dilatation (approx. 11.28%) than initially evolved, 'young' shear bands. Our results agree well with theirs. More importantly, the present result can clarify why the shear-band dilatation (0.5~8%) [49] is below those reported in any earlier study. We note that the dilatation values [49] are associated with the shear-band initiation. However, earlier studies usually performed *ex situ* measurements on mature shear bands. The underlying mechanism can be explained by the following physical picture. At the initial stage of deformation, cooperative rearrangements among atomic clusters take place and the excess

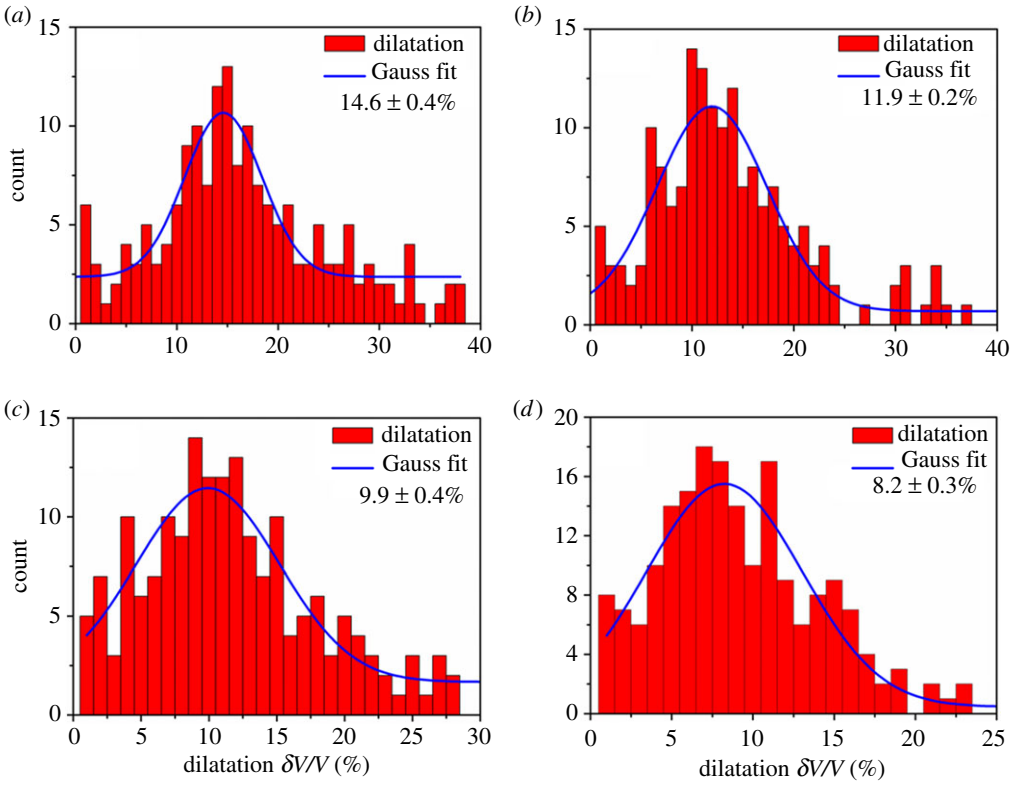

Figure 9. Histograms of values of shear-band dilatancy calculated form AE bursts at different cutting depths. (*a–d*) The depth of 90, 75, 65 and 50 µm, respectively.

free volumes are gathered together to form sub-nano 'defects'. Then the individual nano-voids incubate and grow up. As further developing, the nano-voids prefer to extend their volumes along the shear bands and coalesce with other voids. This limits the diffusion of free volume and keeps the dilatation at a relatively high level. After some nano-voids coalescence, a few micro-cracks will form at different positions along the shear bands. These works further confirm that the dilatancy increases with increasing the evolution degree of shear bands. In the following, we have a detailed discussion on the quantification of this correlation and the influence of dilatancy on the transition of ductile-to-brittle shear bands, through developing an evolution model of shear bands in MGs.

4. Theoretical analysis

(a) Shear-band evolution model

As for machining of crystalline alloys, considerable works focus on the chip formation [44,45]. Based on the momentum diffusion model, theoretically described the evolution of periodic shear bands in the machining of a Ti-based alloy [45]. As for the amorphous alloys, Jiang & Dai [27] developed a coupled thermomechanical orthogonal cutting model to describe the lamellar chip formation. The behaviour of shear-band evolution during MG machining is still lacked. In this regard, we attempt to interpret the dynamics of shear-band evolution by relating atomic-scale deformation process to macroscopic shear-band behaviour. As indicated in figure 10*a*, we assume the tool is in contact with the MG workpiece over an area $A = Cw$, where w is the width of contact and C is the contact length. Experimental observations indicate that C is of the same order of

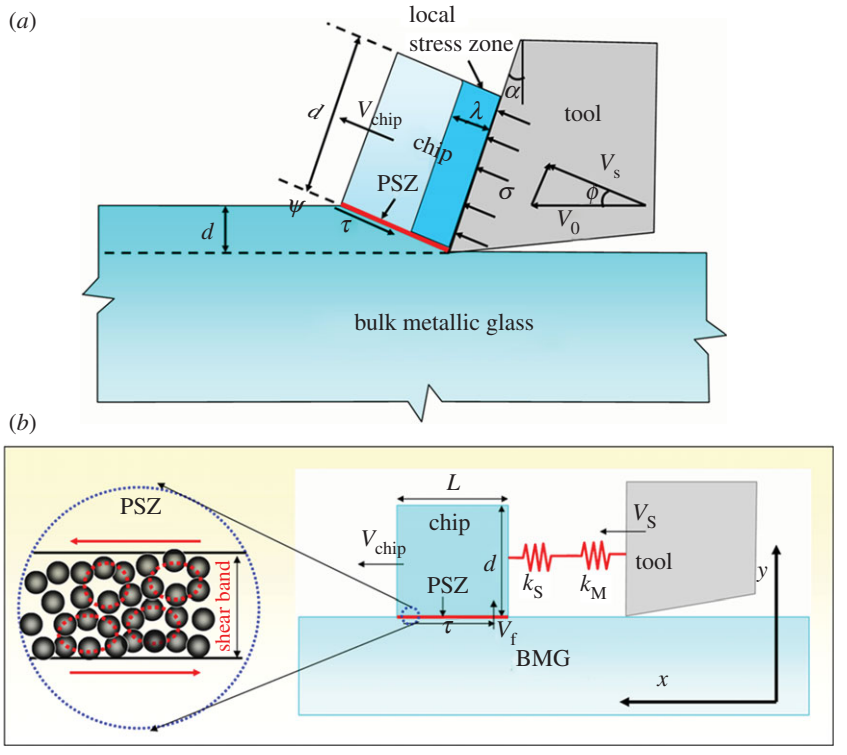

Figure 10. (*a*) One-dimensional shear-band evolution model of orthogonal cutting in the PSZ and (*b*) corresponding equivalent spring slider model with a shear band in the PSZ viewing as cooperative shearing process of a collection of STZs.

magnitude as the depth of cut d. We simplify the geometry by assuming that $\phi = \alpha$, and we neglect the friction and heating caused by it as the chip slides up the tool face due to the low cutting velocity [45]. Thus, we assume the tool exerts a force on the chip over the contact area A in the direction perpendicular to the face of the tool, causing the chip to deform. In the present development, this deformation process is treated as a local compression and there is an elastic stress. Considering that one end of the chip is of extrusion and the other end is stress-free, we introduce a concept of local stress zone to simply characterize the elastic stress distribution of the chip. The elastic stress is concentrated inside the local stress zone with a width λ. The elastic stress gives rise to a shear stress τ to build up in the PSZ. Initially, this shear stress will cause the material in the PSZ to deform elastically, but eventually τ will exceed the yield stress τ_y of the material, and a primary shear band will nucleate in the PSZ. For a material whose deformation hinges upon a shear-banding process, inclusion of the influence of the testing machine besides that of the sample in the study of the mechanical behaviours of the material is inevitable and necessary [52]. To understand the shear-band dynamics, we consider a spring-sliding-block model equivalent to that of orthogonal cutting, as shown in figure 10*b*. A block with a spring of equivalent stiffness $k_S = E\,\mathrm{d}w/\lambda$ (E is the elastic modulus), which represents the chip, is pushed by a spring of stiffness k_M at a constant velocity $V_S = V_0 \cos\phi$, which represents the integrated influence of the tool machine. A thin deformation layer, i.e. the PSZ, lies between the block and MG workpiece. In this workpiece-chip-tool-machine system, three basic equations are obtained via the displacement continuity condition $V_S t - \int_0^t V_{chip}\mathrm{d}t = x_S + x_M$, force-balance condition of two springs $k_M x_M = x_S k_S$ and the kinetic equation of this system $x_S k_S - \tau w L = m\dot{V}_{chip}$, in which V_{chip} and L denote, respectively, the velocity and width of the chip; x_S and x_M are effective compressive displacements of chip and tool-machine springs along the direction x; m is the effective inertia mass of the system.

Substituting the displacement condition and force-balance condition into the kinetic equation, then the kinetic equation can be written as:

$$\frac{k_S k_M}{k_M + k_S}\left(V_S t - \int_0^t V_{chip}\mathrm{d}t\right) - \tau w L = m\dot{V}_{chip}. \tag{4.1}$$

The above equation indicates the material in the PSZ undergoes an elasto-plastic shear deformation during cutting. Initially, this low shear stress τ causes the material in the PSZ to deform elastically. As the τ reaches the yield stress, some local regions in the PSZ preferentially experience shear transformations around high structural disorder. Then shear-band nucleates in these regions, quickly propagates to the free surface, and eventually, a subsequent shearing proceeds in a cooperative manner. It is assumed that, at a time $t = t_1$, shear band starts to slide along the direction x and causes a shear displacement $\psi = \int_{t_1}^{t} V_{chip}\mathrm{d}t$, which is quite large compared with the elastic shear displacement. Therefore, $\psi \approx \int_0^t V_{chip}\mathrm{d}t$ and the governing kinetic equation for this system after activation of the shear band becomes

$$\frac{k_S k_M}{k_M + k_S}(V_S t - \psi) - \tau w L = m\ddot{\psi}, \tag{4.2}$$

where $\ddot{\psi}$ is the second-order time differential of ψ and τ is internal resistant shear stress of the shear band that can be given by the constitutive law of the MGs. Defining the elastic constant $k = k_S k_M/[wL(k_M + k_S)] = \mathrm{d}E/[L\lambda(1+S)]$, where S is defined by $S = k_S/k_M = E\,\mathrm{d}w/(\lambda k_M)$ and called as the compound stiffness, equation (4.2) changes into

$$k(V_S t - \psi) - \tau = M\ddot{\psi} \tag{4.3}$$

with $M = m/(wL)$. Here k and M can be regarded as the stiffness and the inertia of the system per unit area, respectively. From the equation (4.3), one can see that sliding of the shear band in PSZ is determined by the competition between the $k(V_S t - \psi)$ term and the τ term, as the former term reduces the driving stress while the latter one reduces the resistance in the flowing shear band. The stable stop-and-go sliding of the shear band will cause flow serration in the cutting force–displacement curve, while the breaking of stability will result into macroscopic quasi-brittle behaviour. Hence it is necessary to describe the dynamics of shear banding.

Shear banding can be viewed as shear process of a collection of STZs where the constitutive deformation law can be described by the STZ theory. The theory relates the plastic strain rate to the shear stress and internal variables. The macroscopic strain rate in the shear band is proportional to two factors: the strain rate of the individual STZ governed by the shear stress and the number of STZs contained in the band associated with the internal variable. Here we use the cooperative shearing model recently proposed by Johnson & Samwer [53] to describe the behaviour of an individual STZ and some internal variables and to determine the total number of STZs. The cooperative shearing model is mainly based on the concept of inherent states and the potential energy landscape, and considers that the mechanical instability of an STZ is related with the stress-induced destabilization of individual inherent state or local minima of potential energy landscape in MGs. Therefore, a correlation between structure of MGs and their energetics can be well established. The potential energy barrier for an activity of a STZ is biased by an applied shear stress. The inelastic strain rate for an individual STZ spanning the barrier is expressed as:

$$\dot{\gamma} = \dot{\gamma}_s \exp\left(-\frac{W_\tau}{k_B T}\right), \tag{4.4}$$

where $\dot{\gamma}_s$ is the characteristic strain rate for per STZ transition, k_B is the Boltzmann constant, T is the temperature and W_τ is the energy barrier to overcome at a finite shear stress τ. Treating the behaviour of STZs as an Eshelby-type inclusion problem and taking shear-induced dilatancy into consideration [54], it is easily shown that $W_\tau = \Omega(4\zeta_s^2/A - \zeta_s)(\tau_y - \tau)^2/\mu$, where Ω is the volume of an STZ, $A = 2\zeta_s - 4\zeta_d c^2(1+\nu)/[3(1-2\nu)]$, $\zeta_s = 15(1-\nu)/(7-5\nu)$ and $\zeta_d = 1.5(1-\nu)/(1-2\nu)$ are the Eshelby factors for pure shear deformation and a dilatancy, respectively. Thus, equation (4.4) can generally give a constitutive relation of the strain rate $\dot{\gamma}$ as a function of the applied

shear stress τ. However, to fully describe the dynamics of the shear band, we note that $\dot{\gamma}$ is also a function of an internal variable characterizing the structural state of the glass, such as free volume [3,14] or effective disorder temperature [55]. In principle, free volume could be related in important ways to the effective disorder temperature [56]. Spaepen [14] has introduced an important idea by postulating the 'flow defect' density n is directly determined by free volume ξ in the system, via a relation of the form $n \propto \exp(-1/\xi)$. Similarly, Falk & Langer [17] have proposed that the total number of STZs is proportional to the Boltzmann factor $\exp(-1/\chi)$, where χ is the effective disorder temperature. In principle, an STZ as the non-structural defect is roughly analogous to the 'flow defect'. Therefore, the activation of STZs is statistically related to the free-volume concentration [57]. Meanwhile, the free-volume concentration is directly associated with the shear-band dilatancy [36]. Eventually, the free volume is involved and the plastic strain rate in the shear band becomes

$$\dot{\gamma} = \dot{\gamma}_s \exp\left(-\frac{W_\tau}{k_B T}\right) \exp\left(-\frac{1}{\xi}\right). \tag{4.5}$$

Following the self-consistent dynamic free-volume model proposed by Johnson *et al*. [58] and used by Jiang & Dai [59], the free-volume evolution in the shear band can be expressed as:

$$\dot{\xi} = G - H, \tag{4.6}$$

where $G = R\dot{\gamma}$ and $H = (4D/\delta^2 + V_f/\delta)(\xi - \xi_0)$. The first term on the r.h.s. accounts for the production rate G of free-volume concentrate, where G is chosen to be linearly proportional to the plastic shear strain rate and the parameter R describes the molar volume produced by a unit plastic shear strain. The second term H is the flow rate of free-volume concentrate from the shear band to the matrix consisting of diffusivity and convection. The diffusivity that is approximated by a second-order difference over the shear band, should vary with the strain rate, so that $D = \ell^2\dot{\gamma}$, where ℓ is a length scale that corresponds to the radius of an STZ. The convection is that the net inflow is divided by residence time in the shear band; where V_f is the material convection velocity due to chip flow as shown in figure 10*b* and $V_f = V_{0\sin}\phi$. ξ and ξ_0 are free-volume concentrate inside and outside the shear band, respectively.

Uniting equations (4.3), (4.5) and (4.6), the shear-band evolution can be analysed. Guided by the literature data, the values for the material constants are used in our shear-band evolution model. Using the STZ radius as the diffusion length of $\ell = 1$ nm [36] will result in a STZ volume of $\Omega = 4 \times 10^{-27}$ m^{-3}. The parameter c is 0.093 [54] and the Poisson ratio ν is 0.36 [28]. The characteristic strain rate for per STZ transition is $\dot{\gamma}_s = 10^{13}$ s^{-1} [60]. The free-volume parameter $\xi_0 = 0.05$ [28] and the parameter R is 0.027 [61]. The shear-band thickness is taken to be $\delta = 15$ nm [49] and the yield stress of BMG is $\tau_y = 1$ GPa. The cutting velocity is $V_0 = 10\,\mu$m s^{-1} and the width of contact between the tool and the BMG workpiece is $w = 5$ mm. The value for m has been suggested to be between 10 and 100 kg [52]. In this work, we would set $m = 20$ kg. The machine stiffness k_M in the present work is experimentally determined as 6×10^7 N m^{-1} via the compressive load–displacement curve of the testing machine without sample at a loading rate of $10\,\mu$m s^{-1}. The width of the local stress zone is difficult to experimentally determine and is still an open question, which is dependent on the cutting depth, the cutting velocity and the mechanics properties of MG workpiece. But here we shall simply assume that λ is constant and equals 20 µm.

Figure 11 presents the prediction of evolution of sliding speed $\dot{\psi}$, shear displacement ψ and free-volume concentration increment $\xi - \xi_0$ inside the shear band at the different cutting depths, all as a function of shear-band sliding time. For the cutting depth d =50, 65, 75 and 90 µm, the sliding clearly goes through an acceleration–deceleration–stop process (see the velocity plotted in figure 11*a*). When the shear-band stops, the shear displacement as well as the free-volume concentrate increment $\xi - \xi_0$ within the shear band, increases with increasing cutting depth, as shown in figure 11*b*,*c*. Furthermore, the predicted free-volume concentrate increment compares very well with the range observed in experiments for the four different cutting depths as shown in figure 12. In these small cutting depths, the serrated flow is stable and the formation of continuous chips indicates the ductile shear band-dominated macroscopic deformation. However, for the

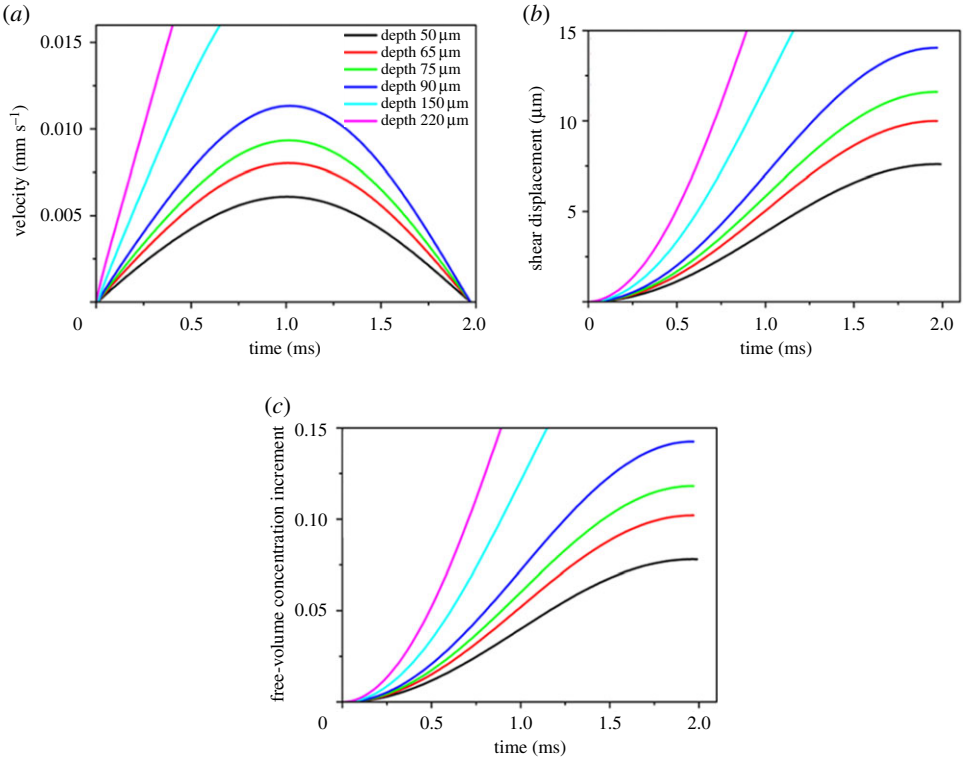

Figure 11. Evolution of (*a*) sliding speed, (*b*) shear displacement and (*c*) free-volume concentrate increment in the shear band at the different cutting depths, all as a function of shear-band sliding time.

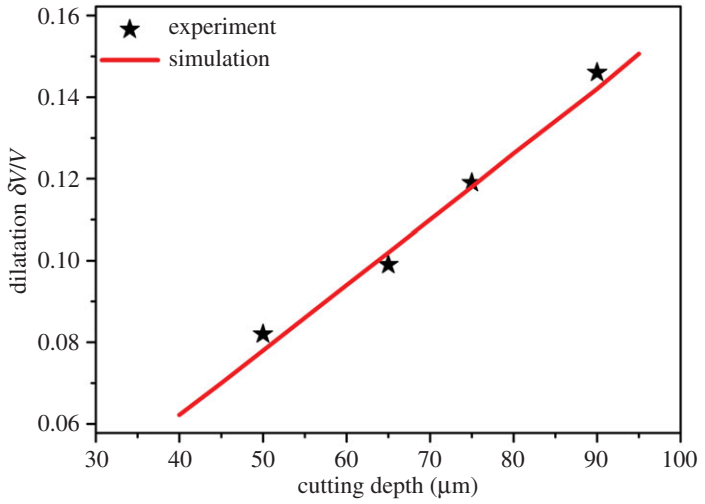

Figure 12. Comparison of the dilatancy of simulation results with those of experimental results.

larger cutting depths with $d = 150$ and 220 µm, both the shear displacement and the free-volume concentrate diverge (not stop), as shown in figure 11*a–c*. Stable serration would then be impossible. Indeed, the formation of discontinuous chips in the cutting depth of 150 and 220 µm shows the runaway failure. The origin of catastrophic instability is the rising dilatancy. For these larger cutting depths, the shear band accelerates continuously (figure 11*a*) and inevitably

turns into a brittle stage during a single sliding event. We confirm an intrinsic correlation between the atomic-scale dilatancy and the dynamics of shear-band evolution, as well as the dilatancy-induced ductile-to-brittle transition of shear bands.

(b) Ductile-to-brittle transition of shear bands

The ductile-to-brittle transition of shear bands, a physically unstable event, can be regarded as the appearance of mathematical instability in the ordinary differential equations governing the shear-band evolution. First, we non-dimensionalize these equations using the following parameters: temperature $T_0 = W_0/k_B$, cutting speed V_0, yield shear stress of the MG τ_y, cutting depth d, where $W_0 = \Omega(4\zeta_s^2/A - \zeta_s)\tau_y$. The parameters can thus be redefined as follows: flow stress $\tilde{\tau} = \tau/\tau_y$, shear displacement $\tilde{\psi} = \tilde{\psi}/d$, plastic strain rate $\dot{\tilde{\gamma}} = \dot{\gamma} d/V_0$,shear-band thickness $\tilde{\delta} = \delta/d$, velocity $\tilde{V}_S = V_S/V_0$ and $\tilde{V}_f = V_f/V_0$, temperature $\tilde{T} = T/T_0$, diffusion length $\ell = \tilde{\ell}/d$, spring constant $\tilde{k} = kd/\tau_y$ and Johnson's damage number $\tilde{M} = (mV_0^2/wLd)/\tau_y$ as indication of shear-band behaviours [62]. The non-dimensional equations are

$$\tilde{k}(\tilde{V}_S\tilde{t} - \tilde{\psi}) - \tilde{\tau} = \tilde{M}\ddot{\tilde{\psi}}, \tag{4.7}$$

$$\dot{\tilde{\gamma}} = \dot{\tilde{\gamma}}_s \exp\left[\frac{-(\tilde{\tau}-1)^2}{\tilde{\mu}\tilde{T}}\right]\exp\left(-\frac{1}{\tilde{\xi}}\right) \tag{4.8}$$

and

$$\dot{\tilde{\xi}} = \tilde{G} - \tilde{H} = R\dot{\tilde{\gamma}} - \left(\frac{4\tilde{\ell}^2\dot{\tilde{\gamma}}}{\tilde{\delta}^2} + \frac{\tilde{V}_f}{\tilde{\delta}}\right)(\tilde{\xi} - \xi_0). \tag{4.9}$$

The instability of shear banding is investigated through a linear perturbation analysis, i.e. seeking an instability solution with respect to small perturbations to the steady solution. The steady solution $(\tilde{V}_c, \tilde{\psi}_c, \dot{\tilde{\gamma}}_c, \tilde{\tau}_c, \xi_c)$ satisfies $(d^2\tilde{\psi}_c/dt^2, d\tilde{\gamma}_c/dt, d\xi_c/dt) = 0$. For small perturbations, it is assumed that $(\delta\tilde{V}, \delta\psi, \delta\tilde{\tau}_f, \delta\dot{\tilde{\gamma}}, \delta\xi) = (V_*, \psi_*, \tau_*, \dot{\gamma}_*, \xi_*)\exp(\alpha t)$, where $(V_*, \dot{\gamma}_*, \psi_*, \xi_*, \tau_*)$ are small constants that characterize the initial magnitude of the perturbation and α is related to the initial rate of growth. The stability of sliding is now determined by the sign of the real part of α: if $\mathrm{Re}(\alpha) < 0$, the sliding is stable; if $\mathrm{Re}(\alpha) > 0$, it is unstable. For later use, let us introduce the notation: $\tilde{\Psi}_{\tilde{V}} = (\partial\tilde{\Psi}/\partial\tilde{V})_c$ (strain rate hardening) and $\tilde{\Psi}_{\xi} = -(\partial\tilde{\Psi}/\partial\xi)_c$ (free-volume softening), where $\tilde{\tau} = \tilde{\Psi}(\dot{\tilde{\gamma}}, \xi)$ is an expression of dimensionless constitutive law. Since $\tilde{G}$ and $\tilde{H}$ are a function of $\dot{\tilde{\gamma}}$, and ξ, we also define the following parameters: $\tilde{G}_{\dot{\tilde{\gamma}}} = (\partial\tilde{G}/\partial\dot{\tilde{\gamma}})_c$ and $\tilde{G}_{\xi} = -(\partial\tilde{G}/\partial\xi)_c$, characterizing the creation rate of ξ due to itself and strain rate; $\tilde{H}_{\dot{\tilde{\gamma}}} = (\partial\tilde{H}/\partial\dot{\tilde{\gamma}})_c$ and $\tilde{H}_{\xi} = (\partial\tilde{H}/\partial\xi)_c$, characterizing the flow rate of ξ due to itself and strain rate. Substituting the instable solution into equations (4.7)-(4.9) and then only considering terms that are of first order in $(\delta\tilde{V}, \delta\psi, \delta\tilde{\tau}_f, \delta\dot{\tilde{\gamma}}, \delta\xi)$, the dimensionless spectral equation for the initial growth rate α of the perturbation is derived by the following form:

$$\alpha^3 + a_1\alpha^2 + a_2\alpha + a_3 = 0, \tag{4.10}$$

where the coefficients of this polynomial are defined by $a_1 = \tilde{\Psi}_{\tilde{V}}/\tilde{M} + (\tilde{H}_{\xi} + \tilde{G}_{\xi})$, $a_2 = \tilde{k}/\tilde{M} + (\tilde{H}_{\xi} + \tilde{G}_{\xi})\tilde{\Psi}_{\tilde{V}}/\tilde{M} - \tilde{\Psi}_{\xi}(\tilde{G}_{\dot{\tilde{\gamma}}} - \tilde{H}_{\dot{\tilde{\gamma}}})/(\tilde{\delta}\tilde{M})$ and $a_3 = (\tilde{H}_{\xi} + \tilde{G}_{\xi})\tilde{k}/\tilde{M}$.

Thus, the question of stability of the linearized problem becomes basically algebraic in nature and investigates the signs of the real part of the roots of spectral equation (4.10). According to Routh–Hurwitz criterion and introducing two new dimensionless variables of $\tilde{M}_N = \tilde{M}/\tilde{\delta}^2\sin\phi$ and $\tilde{k}_N = (1+S)\tilde{k}$, the necessary and sufficient condition for the instability of shear-band sliding is obtained:

$$\Phi(S, \tilde{M}_N) = \left[\frac{(1+S)(\tilde{M}_N P + 1)Q}{\tilde{k}_N}\right] > 1, \tag{4.11}$$

where $\Phi(S, \tilde{M}_N)$ is defined as an instability index; $P = (\tilde{H}_{\xi} + \tilde{G}_{\xi})\tilde{\delta}^2\sin\phi/\tilde{\Psi}_{\tilde{V}}$ and $Q = (\tilde{G}_{\dot{\tilde{\gamma}}} - \tilde{H}_{\dot{\tilde{\gamma}}})\tilde{\Psi}_{\xi}/\tilde{\delta} + \tilde{\Psi}_{\tilde{V}}(\tilde{G}_{\xi} + \tilde{H}_{\xi})$. It can be readily seen from (4.11) that the instability index depends on the external variables (compound stiffness S and the damage number $\tilde{M}_N$), but also the intrinsic

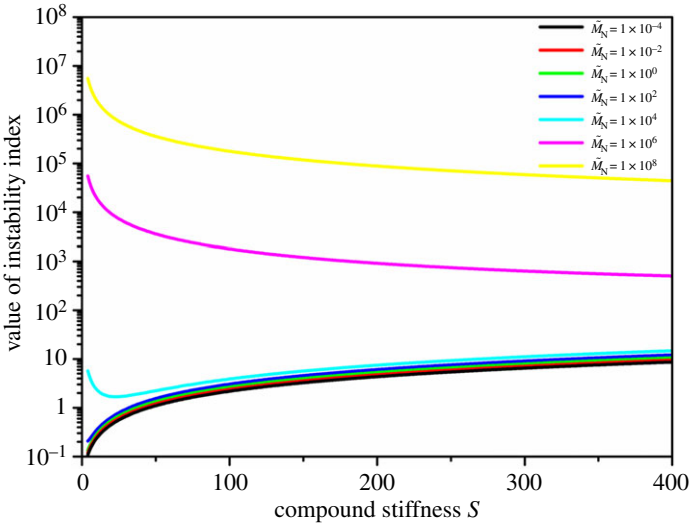

Figure 13. Compound stiffness S and damage number $\tilde{M}_N$ dependence of instability phase diagram of shear-band sliding.

variables which consist of the creation of free volume ($\tilde{G}_{\xi}, \tilde{G}_{\dot{\gamma}}$), and flow of free volume ($\tilde{H}_{\xi}, \tilde{H}_{\dot{\gamma}}$), the strain rate hardening $\tilde{\Psi}_{\tilde{V}}$ and free-volume softening $\tilde{\Psi}_{\xi}$. Consider that these intrinsic variables also are decided by the two external variables. Therefore, the stable shear banding is controlled by the compound stiffness S and the damage number $\tilde{M}_N$, where the former indicates the critical size scales with the machine stiffness of the test machine and the latter suggests the critical velocity scales with the shear strength of MGs. For $\Phi < 1$, the initial perturbation on the shear-band sliding will decay with time, consequently, the sliding of shear bands is stable and shear bands exhibit the ductile behaviour, leading to the macroscopic serrated chips. Conversely, for $\Phi > 1$, the small initial perturbation grows exponentially and results into instability of the sliding, where the shear bands as a runaway shear appear brittle feature and lead to the discontinuous chips. Therefore, the ductile–brittle transition of shear bands occurs at the critical condition of $\Phi = 1$.

The plastic deformation through shear banding is recognized as an instability process, which has been demonstrated to be characterized by the shear-band instability index (SBI), proposed by Han *et al.* [22]. The SBI is controlled by the sample size and the machine stiffness, providing key ingredients to understand the shear-band dynamics of BMGs.

Here, we propose an instability index Φ to characterize the observed ductile-to-brittle transition of shear bands during the cutting of MGs. This instability index is controlled by the compound stiffness and Johnson's damage number. The compound stiffness is proportional to sample size (the cutting depth of MGs) and inversely proportional to machine stiffness. The Johnson damage number is proportional the kinetic energy of the workpiece-chip-tool-machine system and inversely proportional to the material yield strength. Based on equation (4.11), a map for the transition can be plotted as a function of S and $\tilde{M}_N$, as shown in figure 13, where S increases with cutting depths ranging from 20 to 1000 µm at a fixed equivalent machining stiffness $k_M = 6 \times 10^7\,\mathrm{N\,m^{-1}}$, and $\tilde{M}_N$ increases with the cutting velocity ranging from 10^{-6} to $10\,\mathrm{m\,s^{-1}}$. For $\tilde{M}_N < 10^4$, corresponding to the cutting velocity less than $10^{-2}\,\mathrm{m\,s^{-1}}$, the transition occurs as S increases to a critical value and the instability is solely dominated by S. In this situation, these two instability indexes are of the same physical connotation despite the different load conditions (compression and cutting). However, for $\tilde{M}_N > 10^4$, corresponding to the cutting velocity is more than $10^{-2}\,\mathrm{m\,s^{-1}}$, the instability always occurs no matter how S changes and the $\tilde{M}_N$ as the sole factor determines the process. The instability index is dominated by the Johnson damage number.

Incorporation with the cutting velocity of our experiments, the instability is reduced to $\Phi(S) = (1 + S)Q/\tilde{k}_N > 1$. In order to verify the validity of the instability index, its variation at

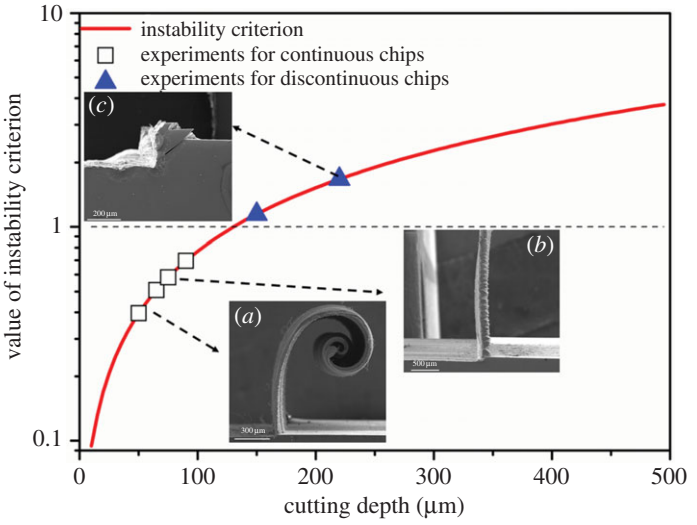

Figure 14. Comparison of instability index Φ with the experimental observations at the different cutting depths.

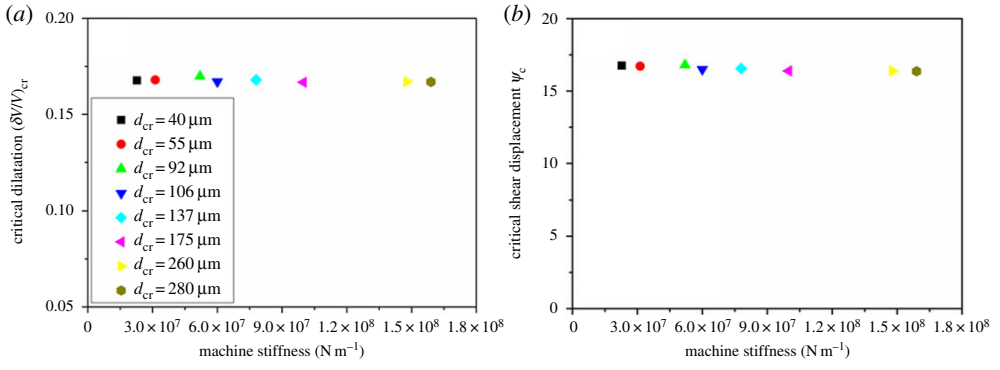

Figure 15. The critical dilatation (*a*) and the critical shear displacement (*b*) under the values of machine stiffness varying from 2.28×10^7 N m^{-1} to 15.9×10^7 N m^{-1}.

the experimentally cutting speed of 10 μm s^{-1} and the machining stiffness of $k_M = 6 \times 10^7$ N m^{-1} is illustrated in figure 14. The ductile or brittle shear band is separated by the critical cutting depth $d_{cr} = 106$ μm, which can be theoretically predicted via $\Phi = 1$. As the cutting depth is smaller than d_{cr}, the deformation of shear bands is stable and ductile behaviour of shear bands induces the serrated chips; otherwise, it is unstable and the discontinuous chips occur. The prediction of instability index is in a good agreement with the experimental results. Therefore, the instability index is valid to predict the ductile-to-brittle transition of shear banding.

Through the instability index, a critical cutting depth d_{cr} associated with the transition of shear banding, can be obtained. And then by combining the d_{cr} with the shear-band evolution model described in section (a), both the free-volume concentrate increase and the shear displacement of a shear band can be calculated. It is a reasonable approximation to take the maximum value of free-volume concentrate increase as the critical dilatancy $(\delta V/V)_{cr}$ associated with the transition of shear bands, as well as the corresponding critical shear displacement ψ_c. Following Han *et al*. [22], we choose the values of machine stiffness k_M varying from 2.28×10^7 N m^{-1} to 15.9×10^7 N m^{-1}. Figure 15*a* show that values of the critical dilatancy $(\delta V/V)_{cr}$ nearly maintain a level of 16.7%, which confirms that the intrinsic dilatancy induces the ductile-to-brittle transition of shear banding, and the critical cutting depth d_{cr} increases with the machine stiffness, which

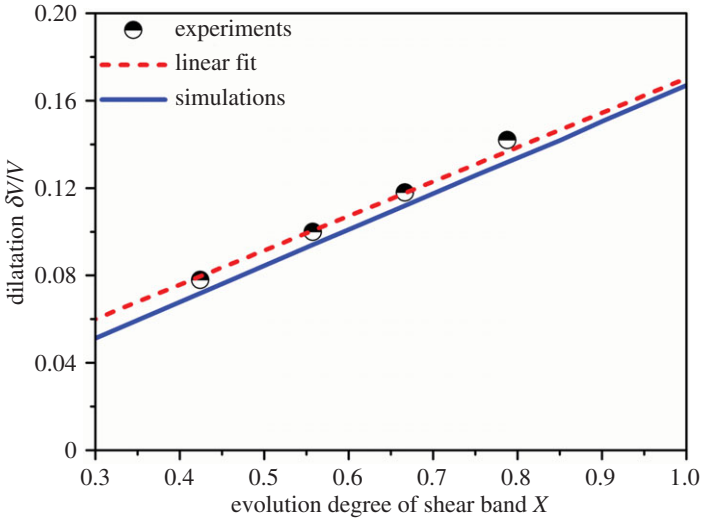

Figure 16. The linear correlation law between the dilatancy $\delta V/V$ and the evolution degree of the shear-band X.

suggests that the higher machine stiffness retards instability. Here, the near constant value of critical shear displacement $\psi_c \sim 16.5\,\mu m$ is obtained under the different machine stiffness, as shown in figure 15*b*. It is commonly assumed that a runaway instability of serrated flow initiates when the shear displacement on a particular shear band reaches a critical value ψ_c. The value of ψ_c depends on the alloy and the loading condition, but is typically taken to be on the order of tens of micrometres [63]. Spaepen and Turnbull have predicted the dilatation limit between 15% (plane stress) and 20% (plane strain) by taking the example of a small edge crack in an amorphous Pd–Si ribbon pulled in tension [64]. Cahn *et al*. have reported that a dilatation was about 15% in a PdCuSi metallic glass subjected to rolling [33]. The critical dilatancy at 16.7%, corresponding to the transition of ductile shear band to brittle shear band, is roughly consistent with these works. In addition, in the machining of metallic glass at the low cutting velocity of $10\,\mu m\,s^{-1}$, the deformation of shear banding can be approximately isothermal via the analysis of the Fourier number *Fo* [65]. Therefore, the temperature rise in a shear band is small and the effect of the temperature rise on the transition can be reasonably ignored.

Noting that a ductile–brittle transition of shear bands occurs when the shear displacement reaches a critical value, we define an important dimensionless parameter $X = \psi/\psi_c (0 \le X \le 1)$, describing the evolution degree of shear bands, in order to uncover the intrinsic relationship between the dilatancy and the evolution degree in shear bands. The case of $X = 0$ implies that the nucleation of shear bands and the case of $X = 1$ indicates an up limit of ductile shear-band evolution and an emergence of the transition. Incorporation of the AE measure results and the evolution of free-volume concentrate using shear-band evolution model, the correlation law between the dilatancy $\delta V/V$ and the evolution degree of the shear-band X is revealed from experiments and simulations in figure 16, where X is calculated via a shear-band evolution model at the different cutting depths. It clearly reveals an increase of dilatancy with an increase of the evolution degree. Moreover, as a shear-band nucleates with zero shear displacement, the corresponding dilatancy of 1.2% is obtained via the linear fitting of experimental results. The predicted dilatancy of 1.2% at $X = 0$, is very close to 2% [49], where they mainly focused on the dilatancy at the shear-band initiation.

5. Conclusion

An ingenious experiment is specially designed to investigate the atomic-scale structure change inside shear bands of MGs. The different evolution degree of the shear band is obtained through

machining with varying the cutting depth, and a quantitative analysis of corresponding AE waveforms gives an *in situ* estimation of the dilatancy or volume change during shear-band evolution. The evolution degree of shear band increases with the increase in cutting depth. A similar relationship between the local volume change and the cutting depth is obtained. It is demonstrated that the degree of dilatancy ranges from 8.2 to 14.6% at the mature stage of shear-band evolution, which is consistent with previous results. Based on the experimental observations, a theoretical model is developed, where the atomic-scale deformation process based on the cooperative shearing model is related to shear-band behaviour. An intrinsic correlation between the atomic-scale dilatancy and the dynamics of shear-band evolution, as well as the dilatancy-induced transition of ductile–brittle shear bands are theoretically reproduced. In the case of small cutting depth, shear bands exhibit the ductile behaviour, leading to the macroscopically serrated chips. However, in the case of larger cutting depths, shear bands as a runaway shearing display the brittle feature and lead to the discontinuous chips. The ductile-to-brittle transition of the shear band is analysed based on the government equations of shear-band evolution dynamics, where the critical local volume dilatancy of 16.7% corresponding to the transition is obtained under the different the values of machine stiffness and the critical cutting depths. These results confirm that the intrinsic dilatancy induces the ductile-to-brittle transition of shear banding. Finally, we reveal that there is a linear scaling relationship between the dilatancy within shear bands and their evolution degree.

Data accessibility. All of the conditions required for duplicating the experiments and analysis have been provided in the manuscript text.

Authors' contribution. L.H.D. designed and supervised the project. F.Z. conducted the experiments. L.H.D. and F.Z. formulated the model and wrote the paper; all authors participated in analysis/interpretation of results, article drafting/editing and critical revisions. All authors approved publication of the final manuscript.

Competing interests. We have no competing interests.

Funding. The work is financially supported by the National Key Research and Development Program of China (no. 2017YFB0702003), the NSFC (grant nos. 11790292, 11472287, and 11522221), the Strategic Priority Research Program of the Chinese Academy of Sciences (grant no. XDB22040302) and the Key Research Program of Frontier Sciences of the Chinese Academy of Sciences (grant no. QYZDJSSW-JSC011).

Acknowledgement. We thank Dr S.L. Cai for the technical assistance of cutting.

Appendix A. Dilatancy model for shear-band evolution

Scruby *et al*. [66] have proposed a suitable method to relate the AE signal to the properties of the corresponding source. Using the point source approximation, the AE source is modelled by a combination of force dipoles D_{ij}, with the subscripts i and j referring to the directions of the forces and their separation, respectively. The AE source relates the AE response to the elastic constants of the material. The surface displacement waveform can be evaluated for each tensor component of a source by using the dynamic elastic Green's tensor relating the displacement at any point in the elastic body to the source. Following these previous work, we assume that dilatancy source during shear banding can be represented by two pairs of force dipoles, D_{11} parallel to the shear band and D_{22} perpendicular to the shear band, as shown in figure 17. The radial displacement at the point (r, θ) from the dipole D_{11} and D_{22} due to the arrival of the compression wave are given by $u_1 = (R_p \sin^2\theta \dot{D}_{11})/[4\pi(\lambda + 2G)c_1 r]$ and $u_2 = (R_p \cos^2\theta \dot{D}_{22})/[4\pi(\lambda + 2G)c_1 r]$, respectively, where $\theta = \pi/2 - \phi$, λ is Lamé's constant, G is the shear modulus, $\dot{D}_{11}$ the time derivative of the source dipole and c_1 is the compression wave speed. The factor R_p takes into account reflection and mode conversion of the incident compression wave at the surface, and $R_p = 2$ in the case of the elastic wave is parallel to the surface normal [49,66].

Thus, the wave-field due to the dilatancy source is given by the sum of the individual contributions: $u = u_1 + u_2 = (\dot{D}_{11}\cos^2\phi + \dot{D}_{22}\sin^2\phi)/[2\pi(\lambda + 2G)c_1 r]$. For a pure dilatancy source, $D_{11} = D_{22} = \delta V(\lambda + 2G/3)$, where δV is the volume change, then the total displacement can reduce to $u = [\delta\dot{V}(\lambda + 2G/3)]/[\pi(\lambda + 2G)c_1 r]$. This relation implies the surface displacement proportional to the rate of volume change $\delta\dot{V}$.

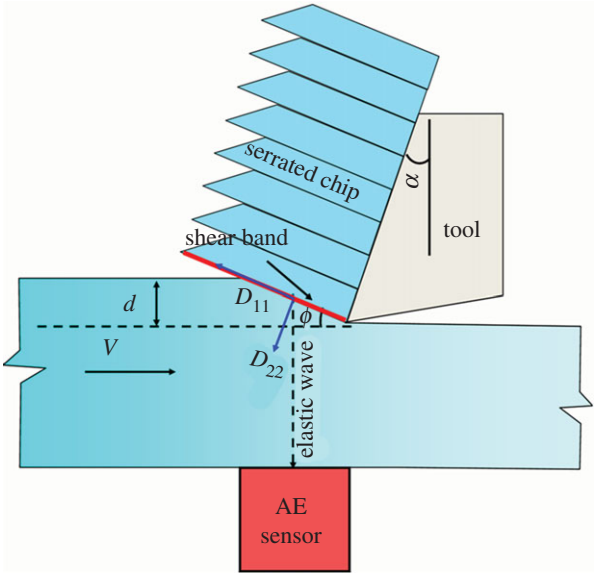

Figure 17. Simplified AE set-up with the AE source (shear band) oriented at an angle ϕ relative to the sensor.

Dilatancy associated with the shear-band process is assumed to be of collective character [49] and its dynamics is reflected in the increasing upper amplitude level during an AE burst (figure 8*c*). Using a linear function in rise time t_r between the first threshold crossing at t_1 and the peak amplitude at t_2, the total volume change from shear-band initiation to shear-band evolution is therefore given by integration of the linear function with respect to time:

$$\delta V = \frac{(\pi c_1 r)(\lambda + 2G)}{\lambda + 2G/3} \int_{t_1}^{t_2} u(t)\,\mathrm{d}t \approx \frac{(\pi c_1 r)(\lambda + 2G)}{\lambda + 2G/3} \frac{kU_p t_r}{2}, \tag{A 1}$$

where k is the sensor calibration factor used to convert the measured amplitude (in volts) into units of surface displacement (metres). Generally, $k = (g_{33}E_x)^{-1}$, where g_{33} is the piezo-electric constant of the sensor with the physical units of $V{\cdot}(\mathrm{m\,N^{-1}})$ and E_x is the elastic modulus ($\mathrm{N\,m^{-2}}$) of the sensor material. Many previous works show that the factor nearly lies about $0.8 \sim 0.2 \times 10^{-12}\ \mathrm{m\,mV^{-1}}$ for a variety of common piezo-electric ceramics, even though g_{33} and E_x are great different among individual ceramics [67–69]. Here $k \sim 0.5 \times 10^{-12}\ \mathrm{m\,mV^{-1}}$ is adopted.

References

1. Ramsay JG. 1980 Shear zone geometry: a review. *J. Struct. Geol.* **2**, 83–99. (doi:10.1016/0191-8141(80)90038-3)
2. Passchier CW. 1984 The generation of ductile and brittle shear bands in a low-angle mylonite zone. *J. Struct. Geol.* **6**, 273–281. (doi:10.1016/0191-8141(84)90051-8)
3. Lemaître A. 2002 Rearrangements and dilatancy for sheared dense materials. *Phys. Rev. Lett.* **89**, 195503. (doi:10.1103/PhysRevLett.89.195503)
4. Schuh C, Hufnagel T, Ramamurty U. 2007 Mechanical behavior of amorphous alloys. *Acta Mater.* **55**, 4067–4109. (doi:10.1016/j.actamat.2007.01.052)
5. Gourlay CM, Dahle AK. 2007 Dilatant shear bands in solidifying metals. *Nature* **445**, 70–73. (doi:10.1038/nature05426)
6. Puzrin AM, Germanovich LN. 2005 The growth of shear bands in the catastrophic failure of soils. *Proc. R. Soc. A* **461**, 1199–1228. (doi:10.1098/rspa.2004.1378)
7. Palmer AC, Rice JR. 1973 The growth of slip surfaces in the progressive failure of over-consolidated clay. *Proc. R. Soc. Lond. A* **332**, 527–548. (doi:10.1098/rspa.1973.0040)
8. Koroknai B, Árkai P, Horváth P, Balogh K. 2008 Anatomy of a transitional brittle–ductile shear zone developed in a low-T meta-andesite tuff: a microstructural, petrological and

geochronological case study from the Bükk Mts. (NE Hungary). *J. Struct. Geol.* **30**, 159–176. (doi:10.1016/j.jsg.2007.10.007)
9. Rolland Y, Cox SF, Corsini M. 2009 Constraining deformation stages in brittle–ductile shear zones from combined field mapping and 40Ar/39Ar dating: the structural evolution of the Grimsel Pass area (Aar Massif, Swiss Alps). *J. Struct. Geol.* **31**, 1377–1394. (doi:10.1016/j.jsg.2009.08.003)
10. Greer AL, Cheng YQ, Ma E. 2013 Shear bands in metallic glasses. *Mater. Sci. Eng. R* **74**, 71–132. (doi:10.1016/j.mser.2013.04.001)
11. Gao YF, Yang B, Nieh TG. 2007 Thermomechanical instability analysis of inhomogeneous deformation in amorphous alloys. *Acta Mater.* **55**, 2319–2327. (doi:10.1016/j.actamat.2006.11.027)
12. Dubois JM, Gaskell PH, Caër GL. 1985 A model for the structure of metallic glasses based on chemical twinning. *Proc. R. Soc. Lond. A* **402**, 323–357. (doi:10.1098/rspa.1985.0121)
13. Reynolds O. 1885 On the dilatancy of media composed of rigid particles in contact, with experimental illustrations. *Philos. Mag.* **20**, 469–481. (doi:10.1080/14786448508627791)
14. Spaepen F. 1977 A microscopic mechanism for steady state inhomogeneous flow in metallic glasses. *Acta Metall.* **23**, 407–415. (doi:10.1016/0001-6160(77)90232-2)
15. Spaepen F. 2006 Metallic glasses: must shear bands be hot? *Nat. Mater.* **5**, 7–8. (doi:10.1038/nmat1552)
16. Argon AS. 1979 Plastic-deformation in metallic glasse. *Acta Metall.* **27**, 47–58. (doi:10.1016/0001-6160(79)90055-5)
17. Falk ML, Langer JS. 1998 Dynamics of viscoplastic deformation in amorphous solids. *Phys. Rev. E* **57**, 7192–7205. (doi:10.1103/PhysRevE.57.7192)
18. Jiang MQ, Wilde G, Chen JH, Qu CB, Fu SY, Jiang F, Dai LH. 2014 Cryogenic-temperature-induced transition from shear to dilatational failure in metallic glasses. *Acta Mater.* **77**, 248–257. (doi:10.1016/j.actamat.2014.05.052)
19. Wang Y-J, Jiang MQ, Tian ZL, Dai LH. 2016 Direct atomic-scale evidence for shear–dilatation correlation in metallic glasses. *Scr. Mater.* **112**, 37–41. (doi:10.1016/j.scriptamat.2015.09.005)
20. Zhang H, Maiti S, Subhash G. 2008 Evolution of shear bands in bulk metallic glasses under dynamic loading. *J. Mech. Phys. Solids* **56**, 2171–2187. (doi:10.1016/j.jmps.2008.01.008)
21. Chen Y, Jiang MQ, Dai LH. 2013 Collective evolution dynamics of multiple shear bands in bulk metallic glasses. *Int. J. Plast.* **50**, 18–36. (doi:10.1016/j.ijplas.2013.03.010)
22. Han Z, Wu WF, Li Y, Wei YJ, Gao HJ. 2009 An instability index of shear band for plasticity in metallic glasses. *Acta Mater.* **57**, 1367–1372. (doi:10.1016/j.actamat.2008.11.018)
23. Pan J, Chen Q, Liu L, Li Y. 2011 Softening and dilatation in a single shear band. *Acta Mater.* **59**, 5146–5158. (doi:10.1016/j.actamat.2011.04.047)
24. Zeng F, Chen Y, Jiang MQ, Lu C, Dai LH. 2015 Dynamic fragmentation induced by network-like shear bands in a Zr-based bulk metallic glass. *Intermetallics* **56**, 96–100. (doi:10.1016/j.intermet.2014.09.008)
25. Gao YF. 2006 An implicit finite element method for simulating inhomogeneous deformation and shear bands of amorphous alloys based on the free-volume model. *Model. Simul. Mater. Sci. Eng.* **14**, 1329–1345. (doi:10.1088/0965-0393/14/8/004)
26. Zhang H, Subhash G, Maiti S. 2007 Local heating and viscosity drop during shear band evolution in bulk metallic glasses under quasistatic loading. *J. Appl. Phys.* **102**, 043519. (doi:10.1063/1.2771043)
27. Jiang MQ, Dai LH. 2009 Formation mechanism of lamellar chips during machining of bulk metallic glass. *Acta Mater.* **57**, 2730–2738. (doi:10.1016/j.actamat.2009.02.031)
28. Jiang MQ, Dai LH. 2009 On the origin of shear banding instability in metallic glasses. *J. Mech. Phys. Solids* **57**, 1267–1292. (doi:10.1016/j.jmps.2009.04.008)
29. Dai LH. 2012 Shear banding in bulk metallic glasses. In *Adiabatic shear localization: frontiers and advances* (eds YL Bai, B Dodd.), pp. 311–361. Waltham, MA: Elsevier.
30. Donovan PE, Stobbs WM. 1981 The structure of shear bands in metallic glasses. *Acta Metall.* **29**, 1419–1436. (doi:10.1016/0001-6160(81)90177-2)
31. Rosner H, Peterlechner M, Kubel C, Schmidt V, Wilde G. 2014 Density changes in shear bands of a metallic glass determined by correlative analytical transmission electron microscopy. *Ultramicroscopy* **142**, 1–9. (doi:10.1016/j.ultramic.2014.03.006)
32. Schmidt V, Rosner H, Peterlechner M, Wilde G, Voyles PM. 2015 Quantitative measurement of density in a shear band of metallic glass monitored along its propagation direction. *Phys. Rev. Lett.* **115**, 035501. (doi:10.1103/PhysRevLett.115.035501)

33. Cahn R, Pratten N, Scott M, Sinning H, Leonardsson L. 1983 Studies of relaxation of metallic glasses by dilatometry and density measurements. *MRS Proc.* **28**, 241. (doi:10.1557/PROC-28-241)
34. Megusar J, Argon AS, Grant NJ. 1982 In *Rapidly solidified amorphous and crystalline alloys* (ed. Kear *et al*.), p. 283. New York, NY: Elsevier.
35. Liu C, Roddatis V, Kenesei P, Maaß R. 2017 Shear-band thickness and shear-band cavities in a Zr-based metallic glass. *Acta Mater.* **140**, 206–216. (doi:10.1016/j.actamat.2017.08.032)
36. Jiang MQ, Wilde G, Dai LH. 2017 Shear band dilatation in amorphous alloys. *Scr. Mater.* **127**, 54–57. (doi:10.1016/j.scriptamat.2016.08.038)
37. Shao Y, Yao K, Li M, Liu X. 2013 Two-zone heterogeneous structure within shear bands of a bulk metallic glass. *Appl. Phys. Lett.* **103**, 171901. (doi:10.1063/1.4826117)
38. Murali P, Narasimhan R, Guo TF, Zhang YW, Gao HJ. 2013 Shear bands mediate cavitation in brittle metallic glasses. *Scr. Mater.* **68**, 567–570. (doi:10.1016/j.scriptamat.2012.11.038)
39. Murali P, Guo TF, Zhang YW, Narasimhan R, Li Y, Gao HJ. 2011 Atomic scale fluctuations govern brittle fracture and cavitation behavior in metallic glasses. *Phys. Rev. Lett.* **107**, 215501. (doi:10.1103/PhysRevLett.107.215501)
40. Yang G, Compton WD, Chandrasekar S. 2015 In situ analysis of flow dynamics and deformation fields in cutting and sliding of metals. *Proc. R. Soc. A* **471**, 20150194. (doi:10.1098/rspa.2014.0758)
41. Guo Y, Efe M, Moscoso W, Sagapuram D, Trumble KP, Chandrasekar S. 2012 Deformation field in large-strain extrusion machining and implications for deformation processing. *Scr. Mater.* **66**, 235–238. (doi:10.1016/j.scriptamat.2011.10.045)
42. Sagapuram D, Viswanathan K, Mahato A, Sundaram NK, M'Saoubi R, Trumble KP, Chandrasekar S. 2016 Geometric flow control of shear bands by suppression of viscous sliding. *Proc. R. Soc. A* **472**, 20160167. (doi:10.1098/rspa.2016.0167)
43. Oxley PLB, Hastings WF. 1977 Predicting the strain rate in the zone of intense shear in which the chip is formed in machining from the dynamic flow stress properties of the work material and the cutting conditions. *Proc. R. Soc. Lond. A* **356**, 395–410. (doi:10.1098/rspa.1977.0141)
44. Recht R. 1964 Catastrophic thermoplastic shear. *J. Appl. Mech.* **31**, 189–193. (doi:10.1115/1.3629585)
45. Ye GG, Xue SF, Jiang MQ, Tong XH, Dai LH. 2013 Modeling periodic adiabatic shear band evolution during high speed machining Ti-6Al-4 V alloy. *Int. J. Plast.* **40**, 39–55. (doi:10.1016/j.ijplas.2012.07.001)
46. Cai SL, Dai LH. 2014 Suppression of repeated adiabatic shear banding by dynamic large strain extrusion machining. *J. Mech. Phys. Solids* **73**, 84–102. (doi:10.1016/j.jmps.2014.09.004)
47. Tvergaard V, Needleman A. 1993 Shear band development in polycrystals. *Proc. R. Soc. Lond. A* **443**, 547–562. (doi:10.1098/rspa.1993.0161)
48. Dalla Torre FH, Klaumunzer D, Maass R, Loffler JF. 2010 Stick-slip behavior of serrated flow during inhomogeneous deformation of bulk metallic glasses. *Acta Mater.* **58**, 3742–3750. (doi:10.1016/j.actamat.2010.03.011)
49. Klaumünzer D, Lazarev A, Maaß R, Dalla Torre F, Vinogradov A, Löffler JF. 2011 Probing shear-band initiation in metallic glasses. *Phys. Rev. Lett.* **107**, 185502. (doi:10.1103/PhysRevLett.107.185502)
50. Cai SL, Chen Y, Ye GG, Jiang MQ, Wang HY, Dai LH. 2015 Characterization of the deformation field in large-strain extrusion machining. *J. Mater. Process. Tech.* **216**, 48–58. (doi:10.1016/j.jmatprotec.2014.08.022)
51. Vinogradov AY, Khonik VA. 2004 Kinetics of shear banding in a bulk metallic glass monitored by acoustic emission measurements. *Phil. Mag. A Phys. Condens. Matter. Struct. Defect. Mech. Prop.* **84**, 2147–2166.
52. Cheng Y, Han Z, Li Y, Ma E. 2009 Cold versus hot shear banding in bulk metallic glass. *Phys. Rev. B* **80**, 134115. (doi:10.1103/PhysRevB.80.134115)
53. Johnson W, Samwer K. 2005 A universal criterion for plastic yielding of metallic glasses with a (T/Tg)2/3 temperature dependence. *Phys. Rev. Lett.* **95**, 195501. (doi:10.1103/PhysRevLett.95.195501)
54. Sun L, Jiang MQ, Dai LH. 2010 Intrinsic correlation between dilatation and pressure sensitivity of plastic flow in metallic glasses. *Scr. Mater.* **63**, 945–948. (doi:10.1016/j.scriptamat.2010.07.011)
55. Langer J, Manning M. 2007 Steady-state, effective-temperature dynamics in a glassy material. *Phys. Rev. E* **76**, 056107. (doi:10.1103/PhysRevE.76.056107)

56. Shi Y, Katz M, Li H, Falk M. 2007 Evaluation of the disorder temperature and free-volume formalisms via simulations of shear banding in amorphous solids. *Phys. Rev. Lett.* **98**, 185505. (doi:10.1103/PhysRevLett.98.185505)
57. Jiang MQ, Wang WH, Dai LH. 2009 Prediction of shear-band thickness in metallic glasses. *Scr. Mater.* **60**, 1004–1007. (doi:10.1016/j.scriptamat.2009.02.039)
58. Johnson WL, Lu J, Demetriou MD. 2002 Deformation and flow in bulk metallic glasses and deeply undercooled glass forming liquids – a self consistent dynamic free volume model. *Intermetallics* **10**, 1039–1046. (doi:10.1016/S0966-9795(02)00160-7)
59. Jiang MQ, Dai LH. 2011 Shear-band toughness of bulk metallic glasses. *Acta Mater.* **59**, 4525–4537. (doi:10.1016/j.actamat.2011.03.075)
60. Daub EG, Klaumünzer D, Löffler JF. 2014 Effective temperature dynamics of shear bands in metallic glasses. *Phys. Rev. E* **90**, 062405. (doi:10.1103/PhysRevE.90.062405)
61. Thamburaja P. 2011 Length scale effects on the shear localization process in metallic glasses: a theoretical and computational study. *J. Mech. Phys. Solids* **59**, 1552–1575. (doi:10.1016/j.jmps.2011.04.018)
62. Johnson W. 1972 *Impact strength of materials*. London, UK: Edward Arnold.
63. Han Z, Li Y. 2009 Cooperative shear and catastrophic fracture of bulk metallic glasses from a shear-band instability perspective. *J. Mater. R.* **24**, 3620–3627. (doi:10.1557/jmr.2009.0442)
64. Spaepen F, Turnbull D. 1974 A mechanism for the flow and fracture of metallic glasses. *Scr. Metall.* **8**, 563–568. (doi:10.1016/0036-9748(74)90070-2)
65. Zehnder AT, Babinsky E, Palmer T. 1998 Hybrid method for determining the fraction of plastic work converted to heat. *Exp. Mech.* **38**, 295–302. (doi:10.1007/BF02410392)
66. Scruby CB, Baldwin GR, Stacey KA. 1985 Characterization of fatigue crack extension by quantitative acoustic-emission. *Int. J. Fract.* **28**, 201–222.
67. Haertling GH. 1999 Ferroelectric ceramics: History and technology. *J. Am. Ceram. Soc.* **82**, 797–818. (doi:10.1111/j.1151-2916.1999.tb01840.x)
68. Saito Y, Takao H, Tani T, Nonoyama T, Takatori K, Homma T, Nagaya T, Nakamura M. 2004 Lead-free piezoceramics. *Nature* **432**, 84–87. (doi:10.1038/nature03028)
69. Agarwal ABL, Frederic Jr, Felbeck DK. 1970 Detection of plastic microstrain in aluminum by acoustic emission. *Metall. Trans.* **1**, 1069–1071.